Enhancing Actuation in Magnetic Soft Actuators: An Inverse Design Framework Incorporating Internal Magnetic Coupling

Zhaoda Du, *Graduate Student Member, IEEE*, Arjun Sharma, Sahibzada Shahroze Umar, and Xiaolong Liu, *Senior Member, IEEE*

***Abstract*—This letter investigates the role of internal magnetic interactions in magnetic soft actuators and introduces a novel framework for their design and optimization. Magnetic soft actuators, composed of soft composites embedded with magnetic particles, enable untethered deformation and actuation under external magnetic fields and hold great potential for robotic applications such as minimally invasive surgery and intervention. Existing design approaches primarily address external field effects and mechanical resistance, often neglecting the contributions of internal magnetic interactions, which are critical to actuator performance. To address this gap, we develop an inverse design methodology that integrates material properties, actuator geometry, and internal magnetic dynamics. By analyzing the interplay between particle volumetric fractions, magnetic moment strengths, and intrinsic properties such as saturation magnetization and coercivity, we propose that internal magnetic coupling can significantly enhance deformation. Rotating-square magnetic metastructures are employed to evaluate actuation behaviors, comparing performance with and without internal coupling. Our findings demonstrate that incorporating internal magnetic interactions into the design process can lead to up to a 36–49% increase in deformation. In addition, the inverse design framework accurately predicted actuator performance, with experimental measurements of relaxed and actuated state deformations matching simulation results within 10%. This study contributes to the field by 1) quantifying the role of internal magnetic interactions in enhancing actuator performance, 2) developing a fabrication process that reliably produces a magnetic soft composite with targeted remanence and Young's modulus, and 3) introducing an optimization framework for predictive actuator design.**

***Index Terms*—Soft robotics, actuators, magnetic devices, inverse design.**

I. Introduction

MAGNETIC soft actuators are soft composites embedded with magnetic particles, designed to deform and recover in response to external magnetic fields, thus delivering untethered actuation force for various robotic applications, such as minimally invasive cardiovascular, neurovascular, and gastrointestinal interventions [1], [2], [3]. The deformation behavior of magnetic soft actuators depends on the distribution of magnetic moments throughout their geometry and their mechanical properties, as the external magnetic field interacts with these moments to generate forces and torques on the soft body. Magnetic moments are determined by the volumetric fraction of magnetic particles and their intrinsic magnetic properties. Compared to soft magnetic particles, which can be easily magnetized and demagnetized when changing external magnetic fields, hard-magnetic particles that have high coercivity [4] are preferred materials for fabricating magnetic soft actuators. Their ability to retain a stable magnetic moment under varying external fields enables predictable and programmable behavior, making them suitable for precise control and repeatability in actuation.

Designing magnetic soft actuators with desired actuation behaviors requires solving an inverse design problem within a defined design space. The design space includes the mechanical properties of soft composites, the actuator's geometric structures, magnetic material characteristics, magnetic moment distribution, boundary conditions, and external magnetic fields, etc. Inverse design problems are typically approached through methods such as topology optimization [5], parameterized design optimization [6], and generative design optimization [7]. Previous studies have used parameterized design optimization to develop soft magnetic beams with time-dependent, prescribed shape deformations for interacting with surrounding media [8], [9]. Additionally, level-set topology optimization has been used to design two-dimensional magnetic soft robots that, under external magnetic actuation, transform into prescribed three-dimensional conformal geometries [10]. The solid isotropic material with penalization method has also been applied to optimize the topological structure of magnetic soft actuators to achieve specific actuation behaviors [11]. Furthermore, optimization-based inverse design approaches have been developed for shape-morphing kirigami systems driven by magnetic actuation [12].

State-of-the-art magnetic actuator design methods focus solely on the interaction between the external magnetic field and the magnetic moments within the actuator structure, considering only the resulting magnetic forces and torques while neglecting internal magnetic interactions. This simplification reduces computational complexity and is valid when the magnetic moments are sufficiently weak and the structure's elasticity dominates. Therefore, the actuation behavior of the system is primarily influenced by the external magnetic actuation and the resistance of the structure to deformation. However, internal magnetic coupling between magnetic moments within magnetic soft actuators

Received 14 February 2025; accepted 17 August 2025. Date of publication 1 September 2025; date of current version 11 September 2025. This article was recommended for publication by Associate Editor C. Majidi and Editor C. Laschi upon evaluation of the reviewers' comments. This work was supported in part by the National Science Foundation under Grant 2512394, in part by Texas Tech University (TTU) HEF New Faculty Startup Fund, and in part by TTU President's STEM Mentoring Academy Fund. *(Corresponding author: Xiaolong Liu.)*

The authors are with the Department of Mechanical Engineering, Texas Tech University, Lubbock, TX 79409 USA (e-mail: xiaolong.liu@ttu.edu).

Digital Object Identifier 10.1109/LRA.2025.3604707

2377-3766 © 2025 IEEE. All rights reserved, including rights for text and data mining, and training of artificial intelligence and similar technologies. Personal use is permitted, but republication/redistribution requires IEEE permission. See https://www.ieee.org/publications/rights/index.html for more information.

Authorized licensed use limited to: Texas Tech University. Downloaded on March 18,2026 at 02:21:12 UTC from IEEE Xplore. Restrictions apply.

remains largely unexplored [13]. Prior works such as [14], [15] have considered such interactions using dipole-dipole models, but their systems are based on rigid permanent magnets with strong and fixed magnetization. In magnetic soft composites, the situation is more complex: dilution of magnetic particles weakens overall magnetization, which becomes both field-dependent and coupled to deformation. This raises a key question: can internal magnetic interactions still play a significant role in actuation under such low-moment, deformable conditions?

The fundamental mechanics of the dynamic deformation of magnetic soft actuators arise from the interplay between material elasticity and magnetic forces and torques induced by external and internal fields. As the body deforms, the evolving internal magnetic field contributes to the equilibrium condition, which balances mechanical stresses, magnetic effects, and external payloads. Our hypothesis is that even under low-moment, deformable conditions, internal magnetic coupling can significantly amplify actuation by enabling larger deformations and stronger output forces.

The objective of this work is twofold: first, we investigate the role of internal magnetic coupling by analyzing its dependence on material properties and the strength of the magnetic moment within its practically achievable limits. Second, we incorporate these internal interactions into an inverse design process to explore their potential for complementing approaches that rely solely on external magnetic fields. To address these objectives, we used a rotating square metastructure [16] as a soft magnetic actuator, allowing us to study its actuation and deformation behaviors. We developed a method to manufacture magnetic soft composites with specific magnetization and mechanical properties, as determined through simulation. This approach enables the fabrication of composites that match the simulated parameters. We then compare the actuation behaviors with and without considering internal magnetic coupling. Furthermore, we develop a parameterized design optimization method to inverse design magnetic soft actuators with prescribed actuation behaviors, accounting for the effects of internal magnetic interactions.

The main contributions of this work are as follows:

1) We investigate how internal magnetic interactions affect the deformation and actuation behavior of magnetic soft actuators, revealing their dependence on material properties and achievable magnetic moment strengths.
2) We develop a practical fabrication method for magnetic soft composites with custom magnetization and mechanical properties that bridges simulation design and production.
3) We propose a parameterized design optimization framework that incorporates internal magnetic interactions to extend inverse design capabilities to achieve prescribed actuation behaviors.
4) We validate internal magnetic coupling using rotating-square metastructure experiments, which demonstrate its role in enhancing actuation deformation and achieving target behaviors.

II. Mechanics of Magnetic Soft Actuators

A. General Configuration of a Magnetic Soft Actuator

Fig. 1 illustrates a magnetic soft actuator with a general geometrical configuration, magnetic particle distribution (ovals), and magnetization (straight arrows) across subdomains Ω_1 and Ω_2. An external magnetic field, $\mathbf{B}_e$, is applied across the actuator's domain Ω and the surrounding medium Ω_0, causing deformation of the soft body results from magnetic forces and torques. Computational frameworks have been developed to simulate deformation of magnetic soft actuators, characterized by diverse magnetic and mechanical properties [13], [17], [18], [19]. The overarching methodology involves using the total thermodynamic potential, accounting for contributions from both strain and magnetic energy. The stress distributions in the soft body can be represented as functions of the total thermodynamic potential and the deformation gradient, using constitutive equations [20]. The deformation of a magnetic soft actuator is computed by iteratively solving mechanical equilibrium equations [21].

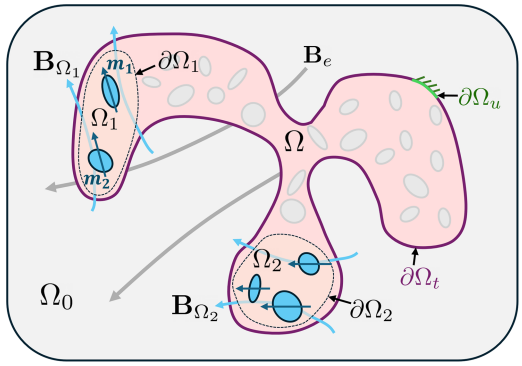

Fig. 1. Conceptual illustration of a magnetic soft actuator in a two-dimensional domain Ω. The domain comprises a soft matrix (pink) embedded with magnetic particles (ovals) and is exposed to an external magnetic field $\mathbf{B}_e$ in the surrounding medium Ω_0. Subdomains Ω_1 and Ω_2 within Ω have distinct magnetization directions (indicated by arrows) and corresponding magnetic moments ($\mathbf{m}_1$ and $\mathbf{m}_2$). These subdomains contribute magnetic fields $\mathbf{B}_{\Omega_1}$ and $\mathbf{B}_{\Omega_2}$ within $\Omega_0 \cup \Omega$. The domain boundary $\partial\Omega$ is partitioned into traction ($\partial\Omega_t$) and displacement ($\partial\Omega_u$) boundaries, with $\partial\Omega_1$ and $\partial\Omega_2$ representing the subdomains.

The soft body deformation is driven by three categories of magnetic energy, as illustrated in Fig. 1: (1) between the external field $\mathbf{B}_e$ and the magnetized particles within Ω; (2) between magnetic fields generated by one subdomain and magnetic moments in another, for example, $\mathbf{B}_{\Omega_2}$ affecting $\mathbf{m}_1$ and $\mathbf{m}_2$ in Ω_1; and (3) between adjacent magnetic particles within the same subdomain, such as the interaction between $\mathbf{m}_1$ and $\mathbf{m}_2$ in Ω_1.

The actuation behavior depends on both the mechanical properties of the soft matrix and the magnetic properties of the particles. Adjacent magnetic dipole interactions become significant with a viscoelastic matrix, strong external fields (e.g., 2 Tesla), or soft-magnetic particles [13]. In contrast, hard-magnetic soft actuators, which exhibit elastic properties [17], [18], operate under external fields below the coercivity, rendering the adjacent magnetic dipole interactions negligible.

Previous studies have predominantly focused on the effect of the first category. However, this research investigates the influence of the second category to determine its relevance in the design of magnetic soft actuators composed of hard-magnetic particles and elastic materials.

B. Modeling Deformation With Helmholtz Free Energy

The total Helmholtz free energy density Ψ of the magnetic soft actuator Ω consists of contributions from the strain energy

Authorized licensed use limited to: Texas Tech University. Downloaded on March 18,2026 at 02:21:12 UTC from IEEE Xplore. Restrictions apply.

density Ψ^s and magnetic energy density Ψ^m:

$$\Psi = \Psi^s + \Psi^m, \tag{1}$$

where $\Psi^s(\mathbf{F})$ is a function of deformation gradient $\mathbf{F}$, and can be explicitly represented by using various constitutive models, such as the Mooney-Rivlin [22] and the neo-Hookean [23], etc. The magnetic energy Ψ^m [24] is formulated as

$$\Psi^m(\mathbf{F}) = -\frac{1}{\mu_0}\hat{\mathbf{B}}_r^{\text{eff}}(\mathbf{F}) \cdot \mathbf{B}_a, \tag{2}$$

where $\hat{\mathbf{B}}_r^{\text{eff}} = J\mathbf{F}^{-1}\mathbf{B}_r^{\text{eff}}$ represents the magnetic soft material's effective magnetic remanence in the reference configuration, with $\mathbf{B}_r^{\text{eff}}$ as the effective remanence in the current configuration. J is the determinant of the deformation gradient $\mathbf{F}$, and μ_0 denotes the permeability of free space.

The applied magnetic field $\mathbf{B}_a$ is defined as the sum of the external magnetic field $\mathbf{B}_e$ and the contributions from internal magnetic fields. Assuming that the internal fields $\mathbf{B}_{\Omega_i}$ are originally defined in the current configuration, we first define their transformation to the reference configuration:

$$\hat{\mathbf{B}}_{\Omega_i} = J\mathbf{F}^{-1}\mathbf{B}_{\Omega_i}, \quad i = 1, \ldots, n, \tag{3}$$

where n is the number of subdomains. Then, the applied magnetic field in the reference configuration is given by

$$\mathbf{B}_a = \mathbf{B}_e + \sum_{i=1}^{n} \hat{\mathbf{B}}_{\Omega_i}. \tag{4}$$

The Cauchy stress tensor, as defined in [20] to describe stress in the current configuration, is expressed as

$$\boldsymbol{\sigma} = J^{-1}\frac{\partial \Psi}{\partial \mathbf{F}}\mathbf{F}^T, \tag{5}$$

which is converted from the first Piola-Kirchhoff stress tensor ($\partial\Psi/\partial\mathbf{F}$) in the reference configuration, and explicitly relates to the deformation gradient $\mathbf{F}$ based on the constitutive model selected for the soft material.

The equilibrium equation of the magnetic soft actuator in Fig. 1 is given by

$$\nabla \cdot \boldsymbol{\sigma} + \mathbf{f}_e = \mathbf{0}, \quad \text{in } \Omega, \tag{6}$$

with boundary conditions

$$\mathbf{u} = \mathbf{u}_0 \quad \text{on } \partial\Omega_u, \quad \boldsymbol{\sigma} \cdot \mathbf{n} = \mathbf{t}_0 \quad \text{on } \partial\Omega_t, \tag{7}$$

where $\mathbf{u}$ is the displacement field, $\mathbf{f}_e$ represents the external forces applied to the soft body, such as loading or friction; $\mathbf{n}$ is the outward unit normal vector; $\mathbf{u}_0$ represents the prescribed displacement vector on the displacement boundary $\partial\Omega_u$; and $\mathbf{t}_0$ represents the prescribed traction vector on the traction boundary $\partial\Omega_t$.

Solving (6) in Ω involves reformulating the problem as an integral equation by using the weak form approach, which broadens the solutions space to include functions that are integrable rather than strictly differentiable:

$$\int_{\partial\Omega_t} \mathbf{t}_0 \cdot \mathbf{u}\, dS = \int_{\Omega} \boldsymbol{\sigma}(\mathbf{u}) : \nabla \mathbf{u}\, d\Omega - \int_{\Omega} \mathbf{f}_e \cdot \mathbf{u}\, d\Omega, \tag{8}$$

where the displacement field vector $\mathbf{u}$ is both the trial and test function. The solution process minimizes the potential energy of the system ($\int_{\partial\Omega_t} \mathbf{t}_0 \cdot \mathbf{u}\, dS$), which balances the internal strain energy ($\int_{\Omega} \boldsymbol{\sigma}(\mathbf{u}) : \nabla \mathbf{u}\, d\Omega$) against the work done by external forces ($\int_{\Omega} \mathbf{f}_e \cdot \mathbf{u}\, d\Omega$).

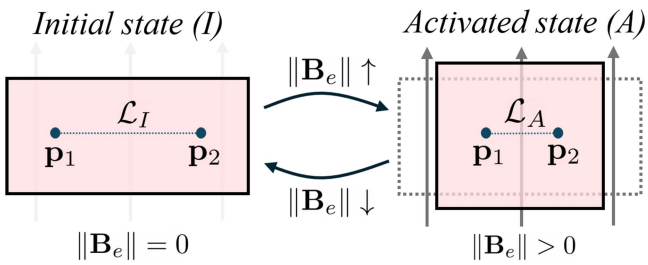

Fig. 2. Illustration of the inverse design problem for a 2-D magnetic soft actuator. The goal is to control horizontal deformation by applying a vertical uniform magnetic field $\mathbf{B}_e$, characterized by the Euclidean distance $\mathcal{L}$ between points $\mathbf{p}_1$ and $\mathbf{p}_2$. Increasing $\mathbf{B}_e$ reduces $\mathcal{L}$, while decreasing $\mathbf{B}_e$ restores the initial state.

III. Inverse Design of Magnetic Soft Actuators

In this section, we introduce an inverse design method to develop a 2-D magnetic soft actuator based on the mechanics described in Section II. This approach considers magnetic interactions both between the external field and the magnetic soft body, and within the internal subdomains of the magnetic soft body itself.

A. 2-D Magnetic Soft Actuator

Fig. 2 illustrates the inverse design problem for a general 2-D magnetic soft actuator, located in the highlighted pink domain. This actuator is designed to undergo horizontal deformation, characterized by $\mathcal{L} = \|\mathbf{p}_1 - \mathbf{p}_2\|$, in response to an externally applied vertical magnetic field, $\mathbf{B}_e$. Initially, when $\|\mathbf{B}_e\| = 0$, the initial deformation $\mathcal{L}$ is set to a predefined initial length, $\mathcal{L}_I$. As the external field's strength increases, the actuator deforms, reducing the distance between points $\mathbf{p}_1$ and $\mathbf{p}_2$. Upon reaching maximum deformation $\mathcal{L}_A \to 0$ and subsequently reducing the magnetic field to zero, the actuator returns to its initial state, $\mathcal{L}_I$, avoiding any permanent deformation due to internal magnetic coupling.

B. Design Parameters and Design Space

The design parameters for the magnetic soft actuator consist of geometric configurations, material properties, the distribution and magnetization of the magnetic particles, and the control field. These parameters are structured into a design vector, $\mathbf{x}$, which is subdivided into four distinct groups. The geometry parameters are denoted by $\mathbf{x}_g = (x_1^g, \ldots, x_{n_g}^g) \in \mathbb{R}^{n_g}$, where n_g is the number of geometric parameters. The material properties are represented as $\mathbf{x}_m = (x_1^m, \ldots, x_{n_m}^m) \in \mathbb{R}^{n_m}$, with n_m being the number of material parameters. The magnetization distribution parameters are represented by $\mathbf{x}_d = (x_1^d, \ldots, x_{n_d}^d) \in \mathbb{R}^{n_d}$, where n_d is the number of magnetization parameters. Lastly, the control field parameter is represented only by its magnitude, $\|\mathbf{B}_e\|$, with its direction always vertical. The comprehensive design vector is expressed as $\mathbf{x} = (\mathbf{x}_g, \mathbf{x}_m, \mathbf{x}_d, \|\mathbf{B}_e\|) \in \mathbb{R}^{n_g+n_m+n_d+1}$.

We will use parameterized metastructures to describe the geometries of magnetic soft actuators, as detailed in Section V. The design space for $\mathbf{x}_g$ is defined by the specific domain of the actuator. Rather than accounting for the individual properties of magnetic and soft materials, we parameterize the effective properties of the composite material. This includes essential

Authorized licensed use limited to: Texas Tech University. Downloaded on March 18,2026 at 02:21:12 UTC from IEEE Xplore. Restrictions apply.

mechanical characteristics like Young's modulus E_{comp} and effective magnetic remanence B_r^{eff}. We establish the design space for E_{comp} and B_r^{eff} by calculating their maximum and minimum values. In Section IV, we present a method for computing the volumetric fraction of each component material to achieve the desired E_{comp} and B_r^{eff}. We use hard-magnetic particles that are magnetized to saturation to achieve their maximum magnetic remanence. The magnitude of the control field is limited to within the range of coercivity to avoid demagnetization of magnetic soft actuators.

C. Problem Formulation

Based on the actuation behavior described in Section III-A and the corresponding design parameters and spaces in Section III-B, the inverse design problem is formulated by minimizing three objective functions (9). f_I, $f_{I\to A}$, and $f_{A\to I}$ are defined in (10), (11), and (12). The function f_I quantifies the geometric discrepancy between the actual configuration $\mathbf{u}(\mathbf{x})$ and the initial configuration $\mathbf{u}_I(\mathbf{x})$ of the magnetic soft actuator under zero external field ($\|\mathbf{B}_e\| = 0$), where elastic deformation forces balance internal magnetic coupling forces. The function $f_{I\to A}$ represents the discrepancy between the actual actuation distance, defined by $\mathbf{p}_1$ and $\mathbf{p}_2$, and the prescribed actuation distance $\mathcal{L}_A$ under an applied external field, where $\mathcal{L}$ is the observed actuation distance, as illustrated in Fig. 2. The function $f_{A\to I}$ describes the geometric discrepancy between the actual configuration $\mathbf{u}(\mathbf{x})$ and the initial configuration $\mathbf{u}_I(\mathbf{x})$ when the external field is reduced to zero. The optimization ensures that actuation avoids rotational motion, as required by the constraint in (13). Design parameters are explored within their defined upper and lower bounds, $\mathbf{x}_{ub}$ and $\mathbf{x}_{lb}$, specified in (14).

$$\underset{\mathbf{x}}{\text{Minimize}} \quad f_I, f_{I\to A}, f_{A\to I} \tag{9}$$

$$f_I(\mathbf{x} \mid \|\mathbf{B}_e\| = 0) = \int_\Omega \|\mathbf{u}(\mathbf{x}) - \mathbf{u}_I(\mathbf{x})\|^2 \, d\Omega \tag{10}$$

$$f_{I\to A}(\mathbf{x}) = |\mathcal{L}(\mathbf{x}) - \mathcal{L}_A|^2 \tag{11}$$

$$f_{A\to I}(\mathbf{x} \mid \|\mathbf{B}_e\| \to 0) = \int_\Omega \|\mathbf{u}(\mathbf{x}) - \mathbf{u}_I(\mathbf{x})\|^2 \, d\Omega \tag{12}$$

$$\text{s.t.} \quad \int_\Omega (\nabla \mathbf{u}(\mathbf{x}) - (\nabla \mathbf{u}(\mathbf{x}))^T) \, d\Omega = 0 \tag{13}$$

$$\mathbf{x}_{lb} \le \mathbf{x} \le \mathbf{x}_{ub} \tag{14}$$

D. Computational Strategy

The computation strategy for the parameterized inverse design of the magnetic soft actuator employs the Non-dominated Sorting Genetic Algorithm II (NSGA-II) framework [25]. This method is effective for multi-objective optimization, addressing the three design objectives. NSGA-II was chosen for its ability to efficiently explore nonlinear design spaces and identify Pareto-optimal solutions, ensuring a thorough exploration of the parameter space. The Pareto front represents a set of trade-off solutions among the three objective functions, where no objective can be improved without compromising another. Convergence is promoted through elitism and diversity preservation and is evaluated quantitatively, as discussed in Section V-C, where this strategy is applied to a case study involving the design of a rotating-square metastructure.

IV. Fabrication Method for Specified Magnetic and Mechanical Properties

This section describes the fabrication strategies for magnetic soft actuators designed to meet the optimal magnetic and mechanical properties identified through inverse design. We focus on achieving the desired effective magnetic remanence, B_r^{eff}, and Young's modulus, E_{comp}, by tailoring the material composition. In addition, we introduce a method to determine the maximum volumetric fraction, $\phi_{\max}$, of magnetic particles, which in turn determines the upper bound of B_r^{eff}. The volumetric fraction ϕ is expressed as

$$\phi = \frac{w_{\text{f}}/\rho_{\text{f}}}{w_{\text{f}}/\rho_{\text{f}} + (1 - w_{\text{f}})/\rho_{\text{m}}}, \tag{15}$$

where w_{f} is the ratio of the filler's mass (m_{f}) to the total mass of the composite $w_{\text{f}} = m_{\text{f}}/(m_{\text{m}} + m_{\text{f}})$. m_{m} is the mass of soft polymer matrix. ρ_{f} and ρ_{m} are densities of the filler and the polymer matrix [26].

A. Effective Magnetic Remanence

Effective magnetic remanence B_r^{eff} is the residual magnetization of a magnetic soft composite that results from the combined contributions of the magnetic particles and the soft matrix after removing an external magnetic field. We employ the Kneller–Hawig approach [27] to represent B_r^{eff}:

$$B_r^{\text{eff}}(\phi) = \phi f_\theta B_r, \tag{16}$$

where B_r is the magnetic remanence of the magnetic particles and f_θ is the orientation factor, reflecting the average angle between particle easy axes and the measurement direction; it typically ranges from 0.3–0.6 for random orientations and approaches 1 when fully aligned [28].

B. Young's Modulus

We used the Mori–Tanaka model [29], [30] to estimate the Young's modulus of magnetic soft composites:

$$E_{\text{comp}} = E_{\text{m}} \left[1 + \frac{3\phi \, (E_{\text{f}}/E_{\text{m}} - 1)}{(E_{\text{f}}/E_{\text{m}} + 2) - \phi \, (E_{\text{f}}/E_{\text{m}} - 1)} \right], \tag{17}$$

where E_{m} and E_{f} denote the Young's moduli of the polymer matrix and the magnetic particle fillers, respectively. Compared with the rule of mixtures [31], the Mori-Tanaka model offers an improved estimation of the composite's Young's modulus by integrating the impacts of filler volume percentage and interaction dynamics.

C. Maximal Volumetric Fraction of Magnetic Particles

The maximum volumetric fraction of filler for a soft composite, $\phi_{\max}$, is the highest ratio of filler volume to total composite volume that can be achieved without causing particle agglomeration, void formation, or poor interfacial bonding, all of which ultimately degrade the composite's mechanical properties and processability. The packing density approach is a method to estimate $\phi_{\max}$ for spherical fillers [32]. However, for non-spherical particles (e.g., flake-shaped), $\phi_{\max}$ should be estimated by incorporating an empirical shape correction factor $\eta = S/AR^\beta$, where S is the ratio of the surface area of an equivalent-volume sphere to the particle's actual surface area, AR is the ratio of the longest to the shortest particle dimension, and β is an empirical exponent (typically 0.5–1) quantifying the

Authorized licensed use limited to: Texas Tech University. Downloaded on March 18,2026 at 02:21:12 UTC from IEEE Xplore. Restrictions apply.

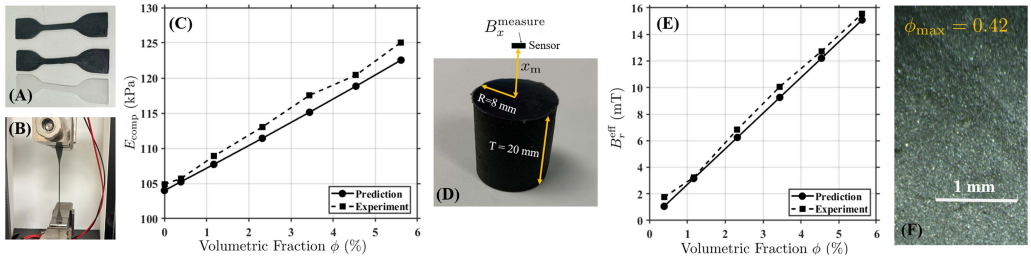

Fig. 3. Experimental validation of the theoretical predictions for the composite Young's modulus E_{comp} and the effective magnetic remanence B_r^{eff}. (a) Dog-bone-shaped magnetic soft composite specimens for measuring E_{comp}. (b) Uniaxial tensile testing. (c) Comparison of experimental and prediction results for E_{comp}. (d) Cylinder-shaped magnetic soft composite specimen for measuring B_r^{eff}. (e) Comparison of experimental and predicted B_r^{eff} values. (f) Microscopic image of a fabricated magnetic soft composite sample with a theoretical maximum volumetric fraction of magnetic particles, $\phi_{max} = 0.42$.

effect of aspect ratio on packing efficiency. The corrected ϕ_{max} is formulated in (18), which typically varies from approximately 0.6 for irregular (non-spherical) particles to around 0.95 for nearly spherical particles [33].

$$\phi_{max} = \eta \cdot \left[\frac{\pi}{N(1-\cos\theta)\sqrt{1+2\cos\theta}} \right], \tag{18}$$

where θ is the angle between the centers of three spheres (with $\theta = 90^\circ$ in cubic packing), and N represents the number of fillers each filler directly contacts (i.e., $N = 6$ in cubic packing). By applying a shape correction factor of $\eta = 0.8$ for flake-shaped magnetic particles, the maximum volumetric fraction is estimated as $\phi_{max} = 0.42$.

V. Experiments and Case Study

A. Magnetic Soft Composite With Prescribed B_r^{eff} and E_{comp}

We validated the fabrication method in Section IV by comparing the predicted and experimental values of Young's modulus E_{comp} and effective magnetic remanence B_r^{eff}. Magnetic soft composite samples were fabricated using Ecoflex 00-50 silicone rubber with a Young's modulus of $E_m = 104\,\text{kPa}$ and density $\rho_m = 1070\,\text{kg/m}^3$, combined with hard-magnetic particles (MQFP-15-7, Magnequench International, LLC) that are approximately $5\,\mu\text{m}$ in size and feature a magnetic remanence of $B_r = 896\,\text{mT}$, intrinsic coercivity $H_{ci} = 582\text{kA/m}$, Young's modulus $E_f = 160\text{GPa}$, and density $\rho_f = 2700\text{kg/m}^3$.

For E_{comp}, we fabricated dog-bone–shaped magnetic soft composite specimens with volumetric fractions ranging from 0% to 5.61% (Fig. 3(a)). Uniaxial tensile tests were performed on an Instron 5966 Universal Testing System (Fig. 3(b)), and the Young's moduli were determined from the stress–strain curves up to 25% strain. Three samples were tested for each volumetric fraction, and the results were averaged. As shown in Fig. 3(c), the model predictions closely match the experimental data.

For B_r^{eff}, we prepared cylindrical magnetic soft composite specimens with volumetric fractions ranging from 0% to 5.61% (Fig. 3(d)). The samples were axially magnetized using a 2T magnetic field (Jiuju MA-2030). To experimentally determine B_r^{eff}, we employed an empirically validated formula [34] that relates axial displacement x_m and the magnetic field $B_r^{measure}$ for axially magnetized, cylinder-shaped magnets:

$$B_x^{measure} = \frac{B_r^{eff}}{2}\left(\frac{x_m + T}{\sqrt{R^2 + (x_m^2 + T)^2}} - \frac{x_m}{\sqrt{R^2 + x_m^2}} \right). \tag{19}$$

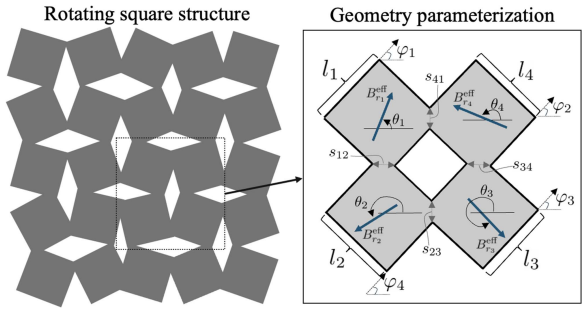

Fig. 4. 2-D magnetic soft actuator with a rotating square structure. Each unit element within the structure is geometrically parameterized by effective magnetic remanences B_{r1}^{eff}, B_{r2}^{eff}, B_{r3}^{eff}, and B_{r4}^{eff}, differentiated across distinct domains. Blue arrows represent the directions of magnetization.

The cylinder-shaped samples had a radius of $R = 8\,\text{mm}$ and a height of $T = 20\text{mm}$. A Gauss meter probe (GM2, AlphaLab, Inc.) was positioned along the axial direction above the cylinder's top surface, at a distance of $x_m = 0.4\text{mm}$, to measure $B_x^{measure}$. Using this measurement, B_r^{eff} was calculated. Fig. 3(e) demonstrates that the theoretical predictions of B_r^{eff} closely match the experimental measurements. In this analysis, the orientation factor f_θ in (16) was set to 0.3, serving as a fine-tuning parameter for the flake-shaped magnetic particles.

We evaluated the integrity of a magnetic soft composite sample fabricated with the theoretical maximum volumetric fraction $\phi_{max} = 0.42$ (see Section IV-C) using an AmScope 3.5X-180X Trinocular microscope. Fig. 3(f) shows that the magnetic particles are uniformly distributed within the soft matrix, with no evidence of agglomeration, void formation, or poor interfacial bonding.

B. Internal Magnetic Coupling in 2-D Magnetic Soft Actuators

We performed finite element (FE) analysis according to Section II to investigate the role of internal magnetic coupling in the deformation of magnetic soft actuators by selectively including or excluding specific terms related to internal magnetic coupling, as indicated in (4). A 2-D rotating square metastructure [35] as shown in the left panel of Fig. 4 was used as a case study. This structure consists of connected squares made of the same magnetic soft composite. For analytical simplification, we considered a unit element that is parameterized in the right panel of Fig. 4: square side lengths $l_1 = l_2 = l_3 = l_4 = 10.7\,\text{mm}$, rotation directions $\varphi_1 = \varphi_2 = \varphi_3 = \varphi_4 = 45^\circ$, magnetization directions $\theta_1 = \theta_4 = 45^\circ, \theta_2 = \theta_3 = 135^\circ$, and connection lengths between squares $s_{12} = s_{23} = s_{34} = s_{41} =$

Authorized licensed use limited to: Texas Tech University. Downloaded on March 18,2026 at 02:21:12 UTC from IEEE Xplore. Restrictions apply.

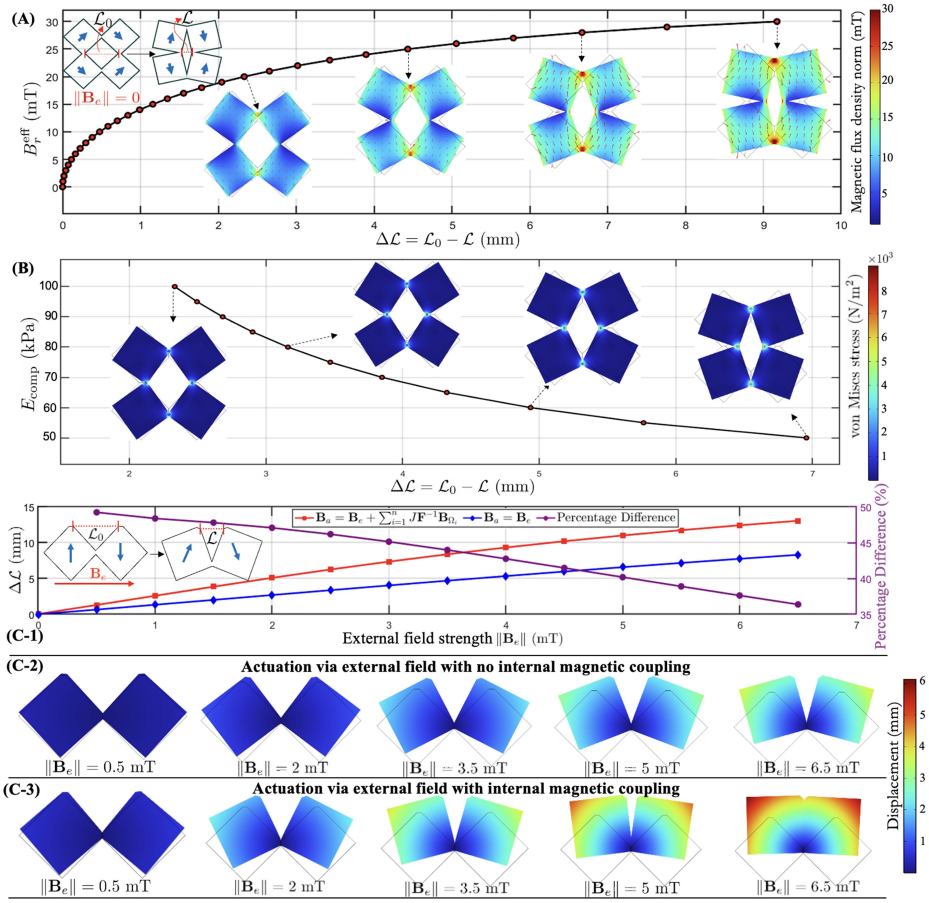

Fig. 5. Impact of internal magnetic coupling on magnetic soft actuator deformation. (a) Increasing the effective magnetic remanence at a fixed composite modulus $E_{\text{comp}} = 100$ kPa triggers a transition from minimal to significant deformation with zero external field applied. (b) A reduction in material stiffness at a fixed effective magnetic remanence $B_r^{\text{eff}} = 20$mT significantly amplifies the deformation response with zero external field applied. (c) Comparison of structural deformation under external field actuation with and without considering internal magnetic coupling.

1 mm. The FE models were implemented in COMSOL Multiphysics version 6.2. The neo-Hookean model was used to describe nearly incompressible hyperelastic mechanical properties [23]. The strain energy function Ψ^s as required in (1) is formulated by

$$\Psi^s = \frac{1}{2}G(I_1 - 3), \tag{20}$$

where the shear modulus is $G \approx E_{\text{comp}}/3$ and $I_1 = \text{tr}(\mathbf{F}^T\mathbf{F})$.

We investigated how internal magnetic coupling deforms the structure in the absence of an external field by varying the effective magnetic remanence, B_r^{eff}, (Fig. 5(a)) and Young's modulus, E_{comp}, (Fig. 5(b)). The deformation, defined as $\Delta\mathcal{L} = \mathcal{L}_0 - \mathcal{L}$, along with the magnetization directions, is illustrated in Fig. 5(a), which also applies to Fig. 5(b).

With $E_{\text{comp}} = 100$ kPa, Fig. 5(a) shows minor deformation ($\Delta\mathcal{L} < 2.5$mm) for $B_r^{\text{eff}} \leq 20$mT, but a significant increase to 9.2mm at $B_r^{\text{eff}} = 30$mT. The color map represents the magnetic flux density norm on the surface, with arrows indicating magnetization directions during deformation. Fig. 5(b) shows that with $B_r^{\text{eff}} = 20$mT, reducing E_{comp} from 100kPa to 50kPa increases deformation from $\Delta\mathcal{L} = 2.3$mm to 6.9mm. The color map represents the von Mises stress distribution.

Fig. 5(c) compares the deformation of a half-element rotating square structure (two connected squares) with and without internal magnetic coupling under an external field $\|\mathbf{B}_e\|$. As described in (4), the internal coupling contribution to the total applied field $\mathbf{B}_a$ is given by $\sum_{i=1}^{n} J\mathbf{F}^{-1}\mathbf{B}_{\Omega_i}$. Fig. 5(c-1) illustrates the half-element rotating square configuration, external field direction, and the comparison of $\Delta\mathcal{L}$ with and without internal coupling under external field strengths ranging from 0mT to 6.5mT. The structure is with $B_r^{\text{eff}} = 60$mT and $E_{\text{comp}} = 400$ kPa.

Fig. 5(c-1) demonstrate that deformation ($\Delta\mathcal{L}$) increases as the external magnetic field strength $\|\mathbf{B}_e\|$ rises, with a more pronounced enhancement when internal coupling is included. Specifically, at $\|\mathbf{B}_e\| = 6$mT, deformation with internal magnetic coupling reaches approximately 12.4mm, compared to around 7.7mm without internal coupling, confirming the significant impact of the internal magnetic contribution on the structural response at the given field strengths. The data indicate that internal magnetic coupling increases deformation by roughly 36–49% compared to the case with only the external field applied. Fig. 5(c-2) and (c-3) visualize the deformations for both cases under varying $\|\mathbf{B}_e\|$.

C. Inverse Design of Magnetic Soft Actuators

We applied the inverse design method described in Section III to design a magnetic soft actuator with a unit element of rotating square structure, as explained in Section V-B. The actuation behavior involves 22 design parameters: 12 for the geometric

Authorized licensed use limited to: Texas Tech University. Downloaded on March 18,2026 at 02:21:12 UTC from IEEE Xplore. Restrictions apply.

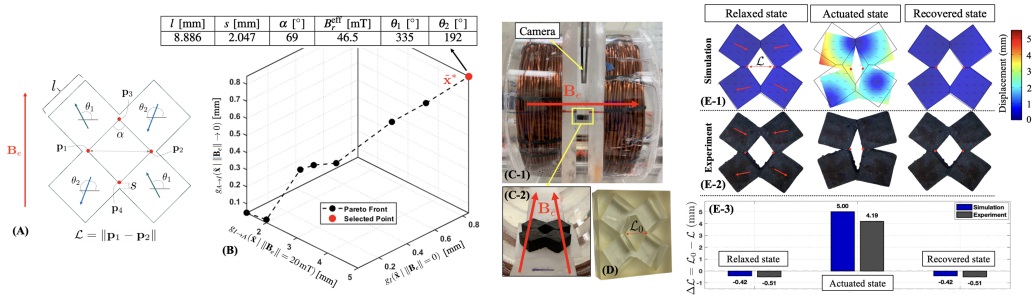

Fig. 6. Optimization of a rotating-square magnetic soft actuator: (a) Design parameters of the actuator; (b) Pareto front for the three objective functions with the optimal solution $\tilde{\mathbf{x}}^*$ highlighted; (c) Experimental setup comprising a one-dimensional Helmholtz coil (C-1) and the fabricated actuator in the workspace (C-2); (d) Mold for fabricating the soft actuator using injection molding; (e) Actuation behavior comparison between simulation and experimental results, including simulation results (E-1), experimental results (E-2), and deformation comparison (E-3).

structure, 8 for the magnetic properties, 1 for the Young's modulus E_{comp}, and 1 for the magnitude of the external magnetic field. To reduce the dimensionality of the design parameters and make the preliminary computational analysis manageable, we simplified the design by considering three primary parameters: the side length l of the square, the connecting length s, and the effective magnetic remanence B_r^{eff}, all of which are treated as uniform across the design. Additionally, due to the symmetric structure, we represent the rotation angles of the squares with a single parameter, α, which corresponds to the rotation angle φ for all squares. The magnetizing directions are assumed to be identical for squares 1 and 3, as well as for squares 2 and 4, with θ_1 and θ_2 used to represent these directions, respectively. Therefore, the design parameter vector is $\tilde{\mathbf{x}} = (l, s, \alpha, B_r^{\text{eff}}, \theta_1, \theta_2, E_{\text{comp}}) \in \mathbb{R}^7$, as illustrated in Fig. 6(a).

$$\underset{\tilde{\mathbf{x}}}{\text{Minimize}} \quad g_I, g_{I\to A}, g_{A\to I} \tag{21}$$

$$g_I(\tilde{\mathbf{x}} \mid \|\mathbf{B}_e\| = 0) = \sum_{i=1}^{4} \|\mathbf{p}_i(\tilde{\mathbf{x}}) - \mathbf{p}_i^I(\tilde{\mathbf{x}})\|^2 \tag{22}$$

$$g_{I\to A}(\tilde{\mathbf{x}} \mid \|\mathbf{B}_e\| = 20\text{mT}) = \|\mathbf{p}_1(\tilde{\mathbf{x}}) - \mathbf{p}_2(\tilde{\mathbf{x}})\|^2 \tag{23}$$

$$g_{A\to I}(\tilde{\mathbf{x}} \mid \|\mathbf{B}_e\| \to 0) = \sum_{i=1}^{4} \|\mathbf{p}_i(\tilde{\mathbf{x}}) - \mathbf{p}_i^I(\tilde{\mathbf{x}})\|^2 \tag{24}$$

$$\text{s.t.} \quad |\mathbf{p}_4^{x_0}(\tilde{\mathbf{x}}) - \mathbf{p}_4^x(\tilde{\mathbf{x}})| < 1\text{mm}, \ \mathbf{p}_1 = \mathbf{p}_1^I \tag{25}$$

$$10^\circ \le \alpha \le 160^\circ, \ 0^\circ \le \theta_1, \theta_2 < 360^\circ \tag{26}$$

$$2\text{mm} \le s \le 5\text{mm}, \ 7\text{mm} \le l \le 10\text{mm} \tag{27}$$

$$22\text{mT} \le B_r^{\text{eff}} \le 80\text{mT}, \ E_{\text{comp}} = 85\,\text{kPa} \tag{28}$$

The general formulation of the multi-objective optimization problem, as described in (9) to (14), for designing magnetic soft actuators is specified in (21) to (28). The function $g_I(\tilde{\mathbf{x}})$ in (22) uses four points, $\mathbf{p}_i$ $(i = 1, \ldots, 4)$ as shown in Fig. 6(a), to describe the initial structure deformation. Here, $\mathbf{p}_i(\tilde{\mathbf{x}})$ denotes the current positions, while $\mathbf{p}_i^I(\tilde{\mathbf{x}})$ represents the prescribed initial positions. $g_{I\to A}(\tilde{\mathbf{x}})$ in (23) represents the Euclidean distance between $\mathbf{p}_1$ and $\mathbf{p}_2$, measuring the actuator's horizontal deformation when an vertical external field of $\|\mathbf{B}_e\| = 20\text{mT}$ is applied. $g_{A\to I}(\tilde{\mathbf{x}})$ in (24) measures the actuator's capability to restore its initial geometry upon removal of the external field. The rotation constraint, as formulated in (25), restricts the motion of $\mathbf{p}_4$ along the x-direction using $\mathbf{p}_4^{x_0}$ as its initial x-coordinate and $\mathbf{p}_4^x$ as its actuated x-coordinate, while also fixing the position of $\mathbf{p}_1$. The design spaces of the design parameters are represented in equations from (26) to (28). We kept E_{comp} at a constant value for this preliminary test.

Fig. 6(b) shows the Pareto front of the optimization problem (21)–(28). As discussed in Section III-D, the NSGA-II algorithm was implemented with a population size of 30 and run for 40 generations to compute the optimal solution for the actuator design. $\tilde{\mathbf{x}}^*$ was selected because it achieves a design with $g_I(\tilde{\mathbf{x}}^* \mid \|\mathbf{B}_e\| = 0) = 1\text{mm}$, $g_{I\to A}(\tilde{\mathbf{x}}^* \mid \|\mathbf{B}_e\| = 20\text{mT}) = 5\text{mm}$, and $g_{A\to I}(\tilde{\mathbf{x}}^* \mid \|\mathbf{B}_e\| \to 0) = 1\text{mm}$. The optimized design parameters are presented in the table in Fig. 6(b).

D. Experimental Evaluation

We used our proposed methods with optimal design parameters to construct the magnetic soft actuator, simulate its actuation, and compare the results with experimental data.

Fig. 6(c-1) shows a one-dimensional Helmholtz coil system that produces a uniform magnetic field from 0 to 500mT across a cubic workspace (700mm per side). Using optimized design parameters, we calculated a volumetric fraction of $\phi = 0.17$ with Ecoflex 00-10 and hard-magnetic MQFP-15-7 particles, resulting in $E_{\text{comp}} = 81.5\,\text{kPa}$. It can be fine-tuned by adding nonmagnetic fillers such as silica powder. The composite was mixed, poured into the mold (Fig. 6(d)), and, after curing, the squares were separated for magnetization, reassembled with additional liquid composite, and cured again. Fig. 6(c-2) shows the actuator's placement in the workspace along with the magnetic field direction.

Figs. 6(e-1) and (e-2) show the simulated and experimental actuation cycles, respectively. The actuator's deformation is defined as $\Delta\mathcal{L} = \mathcal{L}_0 - \mathcal{L}$ with $\mathcal{L}_0 = 8.77\text{mm}$ (see Fig. 6(d)). Fig. 6(e-3) compares the deformation in three states: relaxed ($\|\mathbf{B}_e\| = 0\text{mT}$) with $\Delta\mathcal{L} = -0.42\text{mm}$ (simulation) and $\Delta\mathcal{L} = -0.51\text{mm}$ (experiment); actuated ($\|\mathbf{B}_e\| = 20\text{mT}$) with $\Delta\mathcal{L} = 5\text{mm}$ (simulation) and $\Delta\mathcal{L} = 4.19\text{mm}$ (experiment); and recovered ($\|\mathbf{B}_e\| = 20\text{mT} \to 0\text{mT}$) with $\Delta\mathcal{L} = -0.42\text{mm}$ (simulation) and $\Delta\mathcal{L} = -0.51\text{mm}$ (experiment). The discrepancy in the actuated state is likely due to friction, despite applying lubricant between the actuator and the surface.

VI. Discussion and Conclusion

Determining when internal magnetic interactions significantly affect actuator deformation requires evaluating the interplay among internal magnetic coupling, external magnetic

Authorized licensed use limited to: Texas Tech University. Downloaded on March 18,2026 at 02:21:12 UTC from IEEE Xplore. Restrictions apply.

fields, and elastic restoring torques. Internal magnetic coupling becomes significant when torques arising from interactions between magnetized domains exceed the elastic restoring torques and are comparable to or greater than the torques induced by external fields. In actuators composed of highly compliant materials (Young's modulus in the tens to hundreds of kPa) and densely packed, strongly magnetized hard-magnetic particles, this condition is more likely to be met, making internal interactions non-negligible. In contrast, stiffer actuators (Young's modulus of several MPa or higher) with sparse magnetic particle distributions are less likely to meet this condition, and deformation is dominated by external magnetic fields, allowing internal coupling to be neglected.

Our study confirms this mechanical insight through systematic simulation and experimental validation. First, we observed that incorporating internal magnetic coupling into simulations substantially increased actuator deformation under identical external fields. For example, under an external field of 6mT, the simulated deformation increased from 7.7mm without coupling to 12.4mm when coupling was included, an increase of roughly 36% to 49%. This highlights that neglecting internal interactions can lead to significant underestimation of actuator response. Second, our fabrication process consistently yields magnetic soft composites with target properties, with experiments showing that the measured Young's modulus and effective magnetic remanence closely match our predictions. Third, the inverse design method produces actuator configurations whose performance in simulation agrees well with experimental results. These results demonstrate that careful consideration of internal magnetic interactions and a robust design-to-fabrication process can lead to precise control of actuator behavior for future applications in soft robotics.

Author Contributions

Xiaolong Liu: Conceptualization, Methodology, Software, Investigation, Supervision, Funding, Writing; Zhaoda Du: Methodology, Investigation, Software, Writing; Arjun Sharma: Methodology, Validation, Writing; Sahibzada Shahroze Umar: Software

References

[1] F. Carpi and C. Pappone, "Stereotaxis niobe magnetic navigation system for endocardial catheter ablation and gastrointestinal capsule endoscopy," *Expert Rev. Med. Devices*, vol. 6, pp. 487–498, 2009.

[2] Y. Kim et al., "Telerobotic neurovascular interventions with magnetic manipulation," *Sci. Robot.*, vol. 7, no. 65, 2022, Art. no. eabg9907.

[3] X. Liu, G. J. Mancini, Y. Guan, and J. Tan, "Design of a magnetic actuated fully insertable robotic camera system for single incision laparoscopic surgery," *IEEE/ASME Trans. Mechatron.*, vol. 21, no. 4, pp. 1966–1976, Aug. 2016.

[4] G. Bertotti, "Chapter 2 - Types of hysteresis," in *Hysteresis in Magnetism*. New York, NY, USA: Academic, 1998, pp. 31–70.

[5] M. Y. Wang, X. Wang, and D. Guo, "A level set method for structural topology optimization," *Comput. Methods Appl. Mechan. Eng.*, vol. 192, no. 1, pp. 227–246, 2003.

[6] X. Liu et al., "Surgical planning and optimization of patient-specific fontan grafts with uncertain post-operative boundary conditions and anastomosis displacement," *IEEE Trans. Biomed. Eng.*, vol. 69, no. 11, pp. 3472–3483, Nov. 2022.

[7] S. Oh, Y. Jung, S. Kim, I. Lee, and N. Kang, "Deep generative design: Integration of topology optimization and generative models," *J. Mech. Des.*, vol. 141, no. 11, Nov. 2019, Art. no. 111405.

[8] W. Hu, G. Z. Lum, M. Mastrangeli, and M. Sitti, "Small-scale soft-bodied robot with multimodal locomotion," *Nature*, vol. 554, pp. 81–85, 2018.

[9] J. Wang, D. Wang, L. Dong, M. Zhang, and G. Gu, "Analytical modeling and inverse design of centimeter-scale hard-magnetic soft robots," *IEEE Trans. Automat. Sci. Eng.*, vol. 21, no. 4, pp. 5558–5569, Oct. 2024.

[10] J. Tian et al., "Conformal topology optimization of multi-material ferromagnetic soft active structures using an extended level set method," *Comput. Methods Appl. Mechan. Eng.*, vol. 389, 2022, Art. no. 114394.

[11] C. Wang, Z. Zhao, and X. S. Zhang, "Inverse design of magneto-active metasurfaces and robots: Theory, computation, and experimental validation," *Comput. Methods Appl. Mechan. Eng.*, vol. 413, 2023, Art. no. 116065.

[12] L. Wang, Y. Chang, S. Wu, R. R. Zhao, and W. Chen, "Physics-aware differentiable design of magnetically actuated Kirigami for shape morphing," *Nature Commun.*, vol. 14, no. 1, Dec. 2023, Art. no. 8516.

[13] M. Rambausek, D. Mukherjee, and K. Danas, "A computational framework for magnetically hard and soft viscoelastic magnetorheological elastomers," *Comput. Methods Appl. Mechan. Eng.*, vol. 391, 2022, Art. no. 114500.

[14] E. D. Diller and M. Sitti, "Three-dimensional programmable assembly by untethered magnetic robotic micro-grippers," *Adv. Funct. Mater.*, vol. 24, pp. 4397–4404, 2014.

[15] H. Gu et al., "Self-folding soft-robotic chains with reconfigurable shapes and functionalities," *Nature Commun.*, vol. 14, no. 1, Mar. 2023, Art. no. 1263.

[16] C. Coulais, A. Sabbadini, F. Vink, and M. van Hecke, "Multi-step self-guided pathways for shape-changing metamaterials," *Nature*, vol. 561, pp. 512–515, Sep. 2018.

[17] A. L. Dorfmann and R. W. Ogden, "Nonlinear magnetoelastic deformations of elastomers," *Acta Mechanica*, vol. 167, pp. 13–28, 2004.

[18] R. Zhao, Y. Kim, S. A. Chester, P. Sharma, and X. Zhao, "Mechanics of hard-magnetic soft materials," *J. Mechan. Phys. Solids*, vol. 124, pp. 244–263, 2019.

[19] D. Garcia-Gonzalez, "Magneto-visco-hyperelasticity for hard-magnetic soft materials: Theory and numerical applications," *Smart Mater. Structures*, vol. 28, no. 8, 2019, Art. no. 085020.

[20] G. A. Holzapfel, *Nonlinear Solid Mechanics: A Continuum Approach for Engineering*. Chichester, U.K.: Wiley, 2000.

[21] K.-J. Bathe, *Finite Element Procedures*. Upper Saddle River, NJ, USA: Prentice Hall, 1996.

[22] M. Mooney, "A theory of large elastic deformation," *J. Appl. Phys.*, vol. 11, no. 9, pp. 582–592, 1940.

[23] R. Rivlin, "Large elastic deformations of isotropic materials. I. Fundamental concepts," *Philos. Trans. Roy. Soc. London. Ser. A., Math. Phys. Sci.*, vol. 240, no. 822, pp. 459–490, 1948.

[24] G. Bertotti, "Chapter 3 - Maxwel's equations in magnetic media," in *Hysteresis in Magnetism*. New York, NY, USA: Academic, 1998, pp. 73–102.

[25] K. Deb, A. Pratap, S. Agarwal, and T. Meyarivan, "A fast and elitist multiobjective genetic algorithm: NSGA-II," *IEEE Trans. Evol. Comput.*, vol. 6, no. 2, pp. 182–197, Apr. 2002.

[26] A. K. Kaw, *Mechanics of Composite Materials*. Boca Raton, FL, USA: CRC Press, 2005.

[27] E. F. Kneller and R. Hawig, "The exchange-spring magnet: A new material principle for permanent magnets," *IEEE Trans. Magn.*, vol. 27, no. 4, pp. 3588–3600, Jul. 1991.

[28] B. D. Cullity and C. D. Graham, *Introduction to Magnetic Materials*. Hoboken, NJ, USA: Wiley, 2011.

[29] T. Mori and K. Tanaka, "Average stress in matrix and average elastic energy of materials with misfitting inclusions," *Acta Metallurgica*, vol. 21, no. 5, pp. 571–574, 1973.

[30] A. Fedotov, "Mori-Tanaka experimental-analytical model for predicting engineering elastic moduli of composite materials," *Composites Part B, Eng.*, vol. 232, 2022, Art. no. 109635.

[31] W. D. C. Jr and D. G. Rethwisch, *Materials Science and Engineering: An Introduction*. Hoboken, NJ, USA: Wiley, 2020.

[32] T. A. Ghezzehei and D. Or, "Pore-space dynamics in a soil aggregate bed under a static external load," *Soil Sci. Soc. America J.*, vol. 67, no. 1, pp. 12–19, 2003.

[33] W. Xu, K. Zhang, Y. Zhang, and J. Jiang, "Packing fraction, tortuosity, and permeability of granular-porous media with densely packed spheroidal particles: Monodisperse and polydisperse systems," *Water Resour. Res.*, vol. 58, no. 2, 2022, Art. no. e2021WR031433.

[34] K&J Magnetics, "Surface fields 101." Accessed: Feb. 7, 2025. [Online]. Available: https://www.kjmagnetics.com/blog/surface-fields-101

[35] J. N. Grima, A. Alderson, and K. Evans, "Auxetic behaviour from rotating rigid units," *Physica Status Solidi (b)*, vol. 242, no. 3, pp. 561–575, 2005.

Authorized licensed use limited to: Texas Tech University. Downloaded on March 18,2026 at 02:21:12 UTC from IEEE Xplore. Restrictions apply.